

Lecture 9: Strong Flows

E. J. Hinch

1 Birefringent Strand

1.1 Flow of a FENE fluid past a sphere

In the lecture on stress relaxation, we talked about how an Oldroyd-B fluid deforms as it flows past a rigid sphere. We also discussed the two main shortcomings of the Oldroyd-B model as the Deborah number increases, namely the failure to predict the sudden increase in pressure drop after an initial decrease and long wakes. The infinite extensibility of the Oldroyd-B model renders it useless at high Deborah numbers. However, if the Oldroyd-B model is modified into its finitely extensible counterpart also called the FENE (Finitely Extensible Nonlinear Elastic) model, then strong flow phenomena can be successfully predicted.

Figure 1 has been taken from a finite difference calculation [1] for a sphere falling down a cylinder of FENE fluid. Notice the increase in drag force after an initial decrease. The initial decrease in drag until $De = 1.3$ is captured well by the Oldroyd-B model. Such a decrease occurs due to the elasticity of the microstructure lending itself to the flow and deforming along with it. However, at higher Deborah numbers, the Oldroyd-B continues to deform to infinite lengths. The finite extensibility in the FENE model limits the deformation of the microstructure, leading to an extensional viscosity that adds to the drag experienced by the flow. Figure 2 is a plot of the drag force felt by the falling sphere with increasing Wi [2].

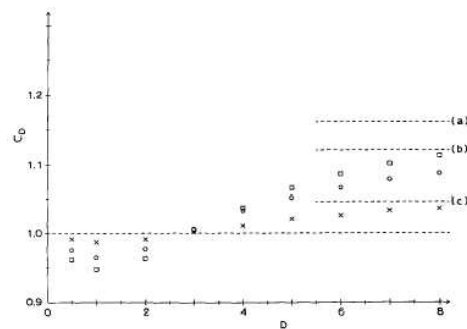


Figure 1: Drag on a sphere with FENE fluid flowing past it plotted against De

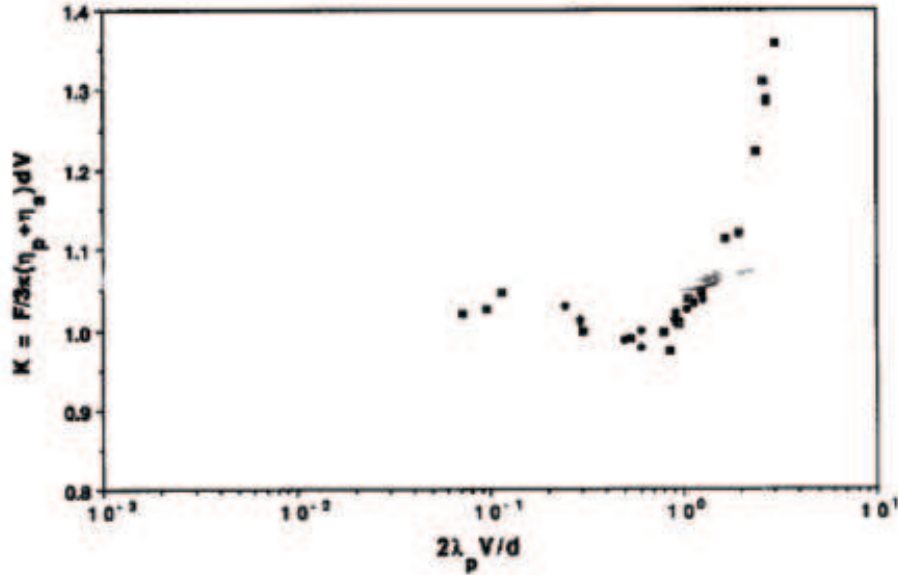


Figure 2: Drag on a sphere in a viscoelastic fluid plotted against Wi , measured experimentally.

It is evident that the Oldroyd-B model does well at small Wi , but fails beyond Wi greater than 1.

FENE calculations also successfully predict the long wake seen in flow past a rigid sphere. The longer-than-Newtonian wake arises because the fluid takes a finite amount of time to relax (relaxation time). The material in the wake is highly stretched due to the strong extensional flow there. Consequently, a large extensional viscosity results that causes increased drag on the sphere above the Newtonian value. It is possible to see these effects by passing polarized light through the medium. As could be predicted from figure 3, very high birefringence is observed in the downstream wake formed by the sphere, especially in the regions close to the center streamline that emanates from the stagnation point. Henceforth, we will refer to this region as the ‘birefringent strand’, and infer that large stresses occur there.

1.2 Cross-slot flow of a viscoelastic fluid

Figure 4 shows the flow of fluid from two channels that are sucked out by two other channels perpendicular to the inlet channels. The velocity profiles at different sections of the exit channel are shown in figures 5 and 7. The flow is simple extensional by design, and will therefore stretch out the microstructure, leading to a birefringent strand. A careful look at the development of the flow profile gives us some confidence about the effect of the birefringent strand on the flow. It is clear that only after a time of the order of the microstructure relaxation time has elapsed, will the parabolic profile develop.

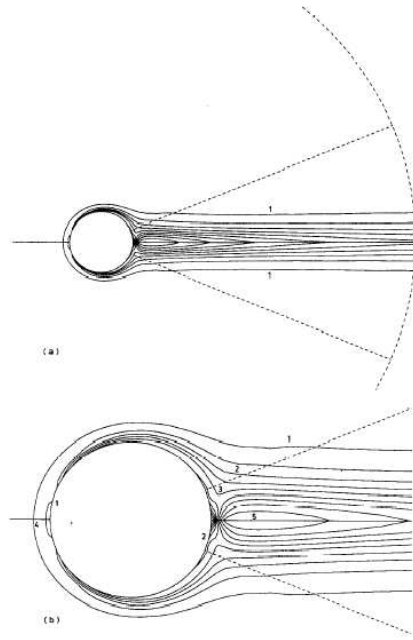


Figure 3: Long wake seen in flow of a FENE fluid past a rigid sphere. The contours are of constant $tr(A)$ [1].

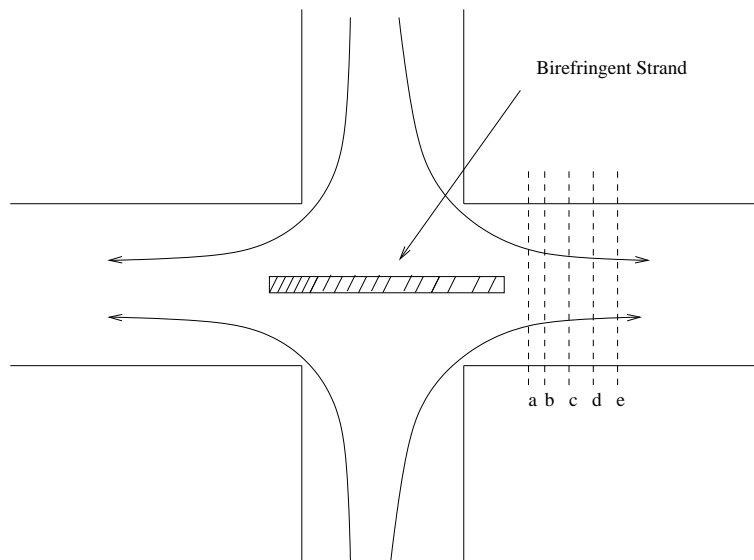


Figure 4: A schematic figure showing the cross-slot flow. The profiles at different positions in the exit channel (a, b, c, d and e) are plotted in the following figure

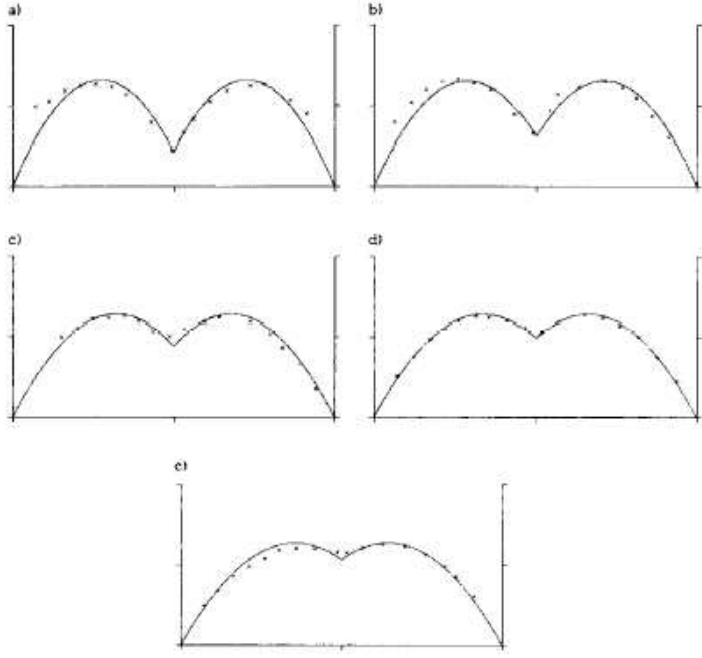


Figure 5: Development of the velocity profile in the exit channel.

This suggests that it is possible to view the birefringent strand in terms of an elastic boundary layer if one views the fluid within this strand as Newtonian but with a very large viscosity equal to the extensional viscosity. In this formulation, the fluid surrounding the strand is imagined to have a constant Newtonian viscosity and the strand is a thin layer of fluid with much higher viscosity.

1.2.1 Analysis of a birefringent strand in an exit channel

The velocity profile in the exit channel is given by

$$u(x, y) = U(x) \frac{a-y}{a} + (Q - U(x)a) \frac{3y(a-y)}{a^2}. \quad (1)$$

Force balance on the birefringent strand results in:

$$\left[\mu \frac{\partial u}{\partial y} \right]_{0^-}^{0^+} + \frac{\partial}{\partial x} \left(\delta \mu_{ext} \frac{\partial U(x)}{\partial x} \right) = 0 \quad (2)$$

where, μ_{ext} is the extensional viscosity in the birefringent strand. From the velocity profile, we have:

$$\left[\mu \frac{\partial u}{\partial y} \right]_{0^-}^{0^+} = 2\mu \left[-\frac{U(x)}{a} + (Q - U(x)a) \frac{3}{a^2} \right] \quad (3)$$

Solving, we obtain

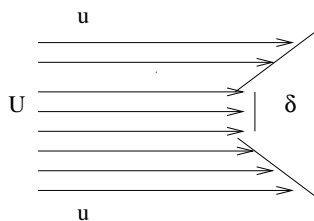
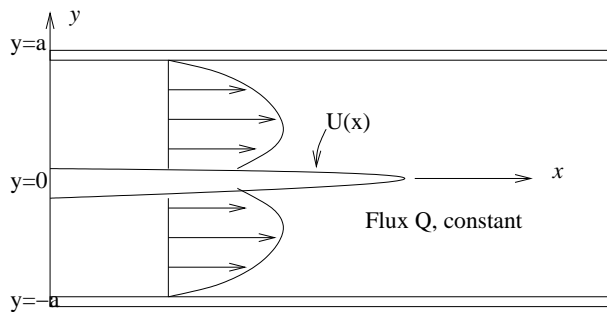


Figure 6: Flow in the exit channel with a birefringent strand

$$U(x) = \frac{3Q}{2a} \left(1 - e^{-\sqrt{\frac{8\mu}{\delta\mu_{ext}a}}x}\right) \quad (4)$$

Thus, the velocity along the center streamline starting at the stagnation point increases very rapidly to the steady Newtonian value. It is also possible to calculate the thickness of the thin birefringent strand (a good exercise for the keen reader). Interesting predictions about the thickness of the birefringent strand for a given flow rate can be made using a FENE dumbbell model for the microstructure. Harlen, Hinch and Rallison [3] performed such calculations and realized that, as the flow rate increased, there must be a transition from thin strands to much thicker ones that would look like pipes. This is shown in figure 7.

1.3 Flow of a FENE fluid past a bubble

Another interesting effect of a stagnation point flow is that of a Non-Newtonian fluid past a bubble. Since the bubble is deformable, unlike a rigid sphere, a cusp forms at the stagnation point. Rallison and Malaga (2003). have worked out the calculations for such a flow. They concluded that the curvature at the cusp becomes sharper with increasing extensibility of the microstructure, as shown by the cartoon in figure 8. By definition, extensibility is ratio of the fully stretched length of the microstructure to its equilibrium size. Note that the curvature increases with stretching of the microstructure, which ultimately leads to elimination of the stagnation point—a nonlinear feedback of the microstructure on the flow.

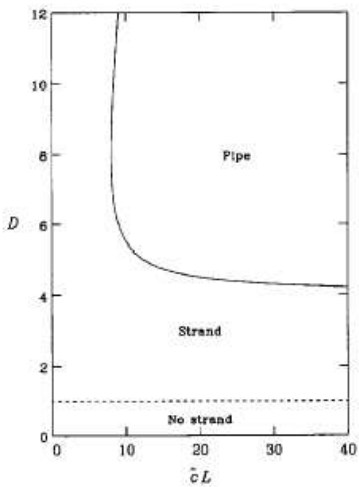


Figure 7: A plot of Deborah number vs concentration of polymer molecules showing the different states of the birefringent strand seen in the numerical calculation.

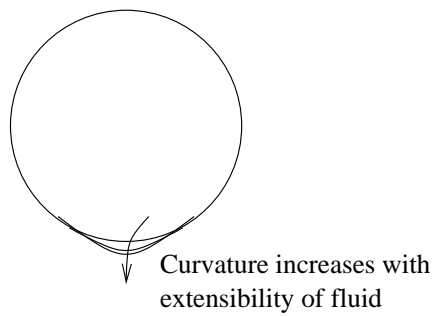


Figure 8: A cartoon of the bubble in a viscoelastic fluid.

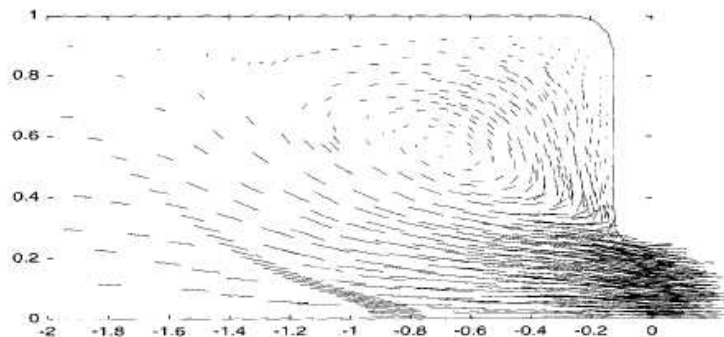


Figure 9: Numerical simulation of a contraction flow of a FENE fluid [4]. Non-Newtonian fluids generate corner vortices that are much larger those apparent in Newtonian fluids.

2 Wine glass model of contraction flow

In lecture 3 we considered anisotropic converging channel flow of a suspension of rigid rods. Here we turn our attention to a strong contraction flow of a general anisotropic material. Experiments and numerical simulations have shown that these flows develop large upstream vortices that have a lengthscale greater than a corner vortex observed in a Newtonian fluid. Figure 9 shows a simulation of flow into a contraction [4] where the large corner vortex is apparent. Figure 10 is an image of a similar contraction flow from experiments [5]. The darker regions outside of the inner flow (white region) are the corner vortices.

We consider the wine glass model of contraction flow, which is a toy model [4]. The geometry is shown in figure 11. Initially there is no deformation of the microstructure in the region upstream of the “wine glass.” In this upstream region the relaxation rate of the microstructure is greater than the strain rate. As we near the contraction, though, the strain rate increases and will become comparable to the relaxation rate. At this transition, material located in the region $r < r_D$ begins to stretch, where r is the distance from the centerline of the pipe (figure 11). Once the fluid passes into the “bowl” of the wine glass, the polymers continue to stretch as both the flow and strain rate increase. Eventually the polymers become fully stretched at a distance r_L from the centerline. At this point the fluid enters the “stem” of the wine glass and travels towards the contraction which has a radius r_C .

We can now make some progress on this problem using scaling arguments. Within the bowl we can approximate the flow as a point sink flow given by

$$u = \frac{Q}{2\pi r^2}. \quad (5)$$

The point sink flow approximation is valid within the bowl and stem regions. Stretching of the microstructure begins to become important when the relaxation rate is of the same order of magnitude as the strain rate, or in other words, the Weissenberg number is $O(1)$. At this point

$$\frac{1}{\tau} \sim E \sim \frac{\partial u}{\partial r} \quad (6)$$



Figure 10: Image of contraction flow from experiments [5]. The white region indicates strong extension flow (the “stem” in the wine glass model), and the corner vortices are the darker regions outside it.

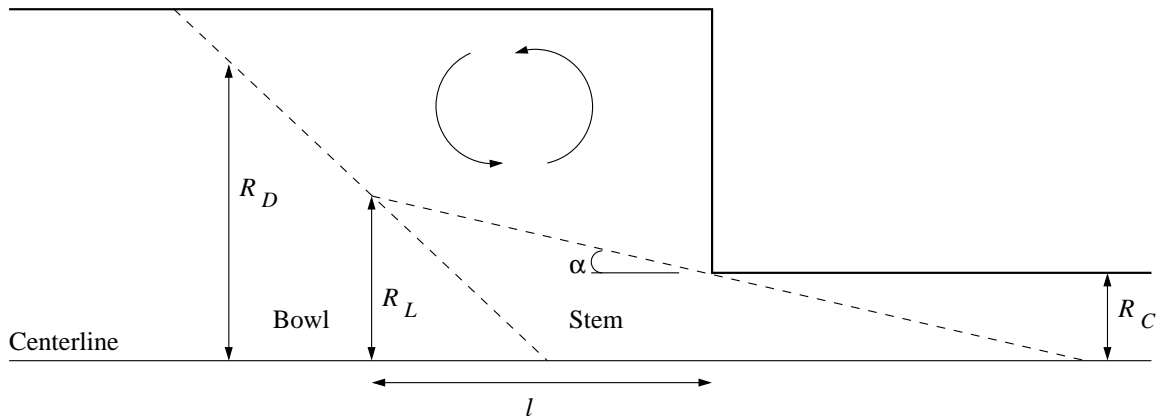


Figure 11: Geometry of the wine glass model of contraction flow [4]. This figure shows half of a pipe with a 4:1 contraction. Flow is into the contraction. The microstructure begins to be stretched once it enters the bowl, and becomes fully stretched when it enters the stem. The maximum radius of the bowl is R_D , the maximum radius of the stem is R_L and the radius of the contraction is R_C .

and, from differentiating (5), we determine that stretching begins to be important at

$$r_D \sim (Q\tau)^{1/3}. \quad (7)$$

Within the bowl, the strain rate becomes large and dominates the relaxation term. In this region then, the microstructure stretches like fluid line elements. Line element stretching is proportional to the velocity of the flow and since A is the tensor describing the microstructure, we find

$$A \propto u^2 \propto r^{-4}, \quad (8)$$

where we have used the relationship between u and r for a point sink flow.

Upon entering the stem of the wine glass, the microstructure has become fully stretched. In this finite extension regime $A \simeq L^2$. Now assuming an individual polymer begins stretching at a distance r_E from the centerline, A at this point is simply equal to 1. Then using (8) we can consider the two limits of undeformed microstructure ($A = 1$) and fully stretched microstructure ($A = L^2$) to show

$$1 \sim \frac{1}{r_E^4}, \quad L^2 \sim \frac{1}{r_L^4}, \quad (9)$$

which gives the result that the microstructure becomes fully stretched at

$$r_L = \frac{r_E}{L^{1/2}}. \quad (10)$$

The large vortices that we are interested in viewing occur only if r_E falls within the region where the strain rate is larger than the relaxation rate. Or in other words, the polymers can only become fully stretched if $r_E = L^{1/2}r_L < r_D$. Note also that this model makes sense only if r_D lies within the upstream pipe. Now applying this constraint and noting that the Deborah number for this flow is given by

$$\text{De} = \frac{Q\tau}{r_C}, \quad (11)$$

we find that the microstructure can become fully stretched only if we exceed a critical Deborah number,

$$\text{De} > \text{De}_{\text{crit.}} = L^{3/2}. \quad (12)$$

In determining $\text{De}_{\text{crit.}}$ we have assumed that $r_L \simeq r_C$, which is true if we assume the cone angle α is small.

Once the material is fully stretched we have an extensional viscosity μ_{ext} that is much larger than the shear viscosity, μ_{shear} , and the momentum balance is between the high extensional viscosity in the stem and the high shear in the recirculating vortices. This balance can be written as

$$\mu_{\text{ext}} \frac{\partial^2 u}{\partial r^2} \simeq \mu_{\text{shear}} \frac{1}{r^2} \frac{\partial^2 u}{\partial \theta^2}. \quad (13)$$

As in the problem we discussed in section 6 from Lecture 3, for converging channel flow, the dependence in the θ direction has a sinusoidal character, where the θ direction is in the

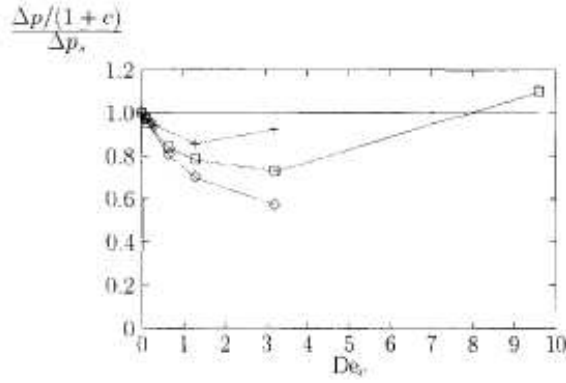


Figure 12: Numerical simulation of pressure drop as a function of Deborah number for an Oldroyd B fluid (Szabo *et al.* 1997). As the Deborah number increases, the microstructure is stretched and the pressure drop decreases. There is some evidence for increasing pressure drop at high De.

direction of the cone angle α . Assuming a separable solution for equation (13), we find that the r -independent solution has a sinusoidal dependence with an argument of $\left(\sqrt{\frac{\mu_{\text{ext}}}{\mu_{\text{shear}}}}\theta\right)$. Therefore the angle of the stem is given by

$$\alpha \sim \sqrt{\frac{\mu_{\text{shear}}}{\mu_{\text{ext}}}}, \quad (14)$$

from which we can see that as long as $\mu_{\text{ext}} \gg \mu_{\text{shear}}$, our assumption of small cone angle is valid. The length of the cone l can be found using trigonometry, $\tan \alpha = (r_L - r_C)/l$, which with the small angle approximation gives

$$l = \frac{r_L - r_C}{\alpha} = r_C \left(\text{De}^{\frac{1}{3}} L^{-\frac{1}{2}} - 1 \right) \sqrt{\frac{G\tau L^2}{\mu}}. \quad (15)$$

Here we have used the fact that $\mu_{\text{ext}} \sim G\tau L^2$ and our previous relationships for r_L and De. It is easy to see from our scaling arguments for the angle α that these vortices are much larger than the corner vortices we would expect to see in a Newtonian fluid. Numerical calculations [4] have shown that these scaling arguments are within 20% of the full numerical calculations. The authors also include numerical models of how the pressure drop varies with increasing Deborah number (figure 12) for an Oldroyd B fluid. As the fluid enters the wine glass and the microstructure is stretched, the pressure drop decreases (cf. turbulent drag reduction). There is also some evidence that at very large Deborah number the pressure drop begins to increase again.

3 Corner singularity

The geometry for flow around a corner singularity is shown in figure 13. For very fast flows around a sharp corner (we will consider a 270° corner), $\nabla u \gg 1/\tau$ or $\text{De} \gg 1$. In this

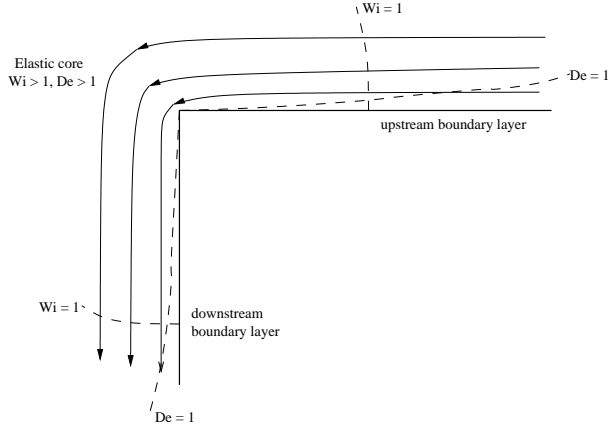


Figure 13: Geometry of flow around a corner singularity. Near the corner, the microstructure is strongly stretched. This region is known as the elastic core. Both upstream and downstream of the corner there will be boundary layers where viscous effects become important (the Deborah number becomes small). Far from the corner the shear is small (the Weissenberg number is small).

case the relaxation of the microstructure is negligible and only the stretching is important. There will be both upstream and downstream boundary layers where the Deborah number is small and viscous effects are important. Also, far from the corner, the shear is small so the Weissenberg number becomes small. The transition between these regions are marked with a dashed line in figure 13. The equation for the evolution of the microstructure in the elastic core then becomes

$$\frac{DA}{Dt} = A \cdot \nabla \mathbf{u} + (\nabla \mathbf{u})^T \cdot A \quad (16)$$

where A deforms with the flow. As we discussed briefly in the previous section and in earlier lectures, the microstructure deforms like fluid line elements. This can be written more formally as

$$\frac{d}{dt} \delta \mathbf{l} = \delta \mathbf{l} \cdot \nabla \mathbf{u}. \quad (17)$$

If we then consider a steady flow, the fact that A will deform like fluid line elements suggests that we look for a solution of the form

$$A = f(\psi) \mathbf{u} \mathbf{u}. \quad (18)$$

Here f is an unknown function which accounts for the fact that the deformation depends on the choice of streamline.

Now when we analyze the momentum equation for these flows, even though the Deborah number is large, the inertial terms are still negligible. Therefore the flow is still Stokes flow except that the stretching of the microstructure GA balances the pressure gradient rather than the viscous forces balancing pressure. Then applying our guess for A and noting that $f(\psi)$ is a scalar function, we can write

$$0 = -\nabla p + G f^{\frac{1}{2}} \mathbf{u} \cdot \nabla f^{\frac{1}{2}} \mathbf{u} \quad (19)$$

where we have used incompressibility, $\nabla \cdot \mathbf{u} = 0$. The reason for splitting f in this fashion is that now equation (19) is suggestive of a steady Euler's equation in $f^{1/2}\mathbf{u}$. Indeed, we can write

$$-\nabla p + \frac{1}{2}G\nabla(f|\mathbf{u}|^2) = 0 \quad (20)$$

and by integrating we get an anti-Bernoulli equation where

$$p - \frac{1}{2}Gf|\mathbf{u}|^2 = \text{const.} \quad (21)$$

along streamlines. This is termed an anti-Bernoulli equation because rather than pressure decreasing with increasing velocity, pressure will increase with increasing velocity. (Theoretically you would need to flip the wings of an airplane upside down to fly in a non-Newtonian fluid!) We can now seek a potential flow solution to (21), assuming the flow is irrotational, and has the form

$$f^{1/2}\mathbf{u} = \nabla\phi. \quad (22)$$

The solution to potential flow around an angle α [6] is

$$\phi = Cr^{\pi/\alpha} \cos\left(\frac{\pi\theta}{\alpha}\right). \quad (23)$$

For our 270° corner with a properly normalized velocity, this gives

$$\phi = \frac{3}{2}r^{\frac{2}{3}} \cos\left(\frac{2}{3}\theta\right). \quad (24)$$

Note that this solution can be obtained by finding the complex potential solution for flow in a half plane and using conformal mapping to transform the flat plate to the desired angle. This now represents the solution for our flow around a corner neglecting the boundary layer effects (i.e. potential flow only satisfies conditions of no normal flow at the boundaries, not the no-slip condition). This also shows that $u \propto \phi/r \propto r^{-1/3}$ and, since $\sigma \propto A \propto u^2$, we find that

$$\sigma \propto r^{-\frac{2}{3}}. \quad (25)$$

At this point, using the definition of the stream function we can write

$$f^{\frac{1}{2}}\mathbf{u} = f^{\frac{1}{2}}(\psi)\nabla \times (0, 0, \psi) = f^{\frac{1}{2}}\nabla \times \left(0, 0, \frac{3}{2}r^{\frac{2}{3}} \sin\frac{2}{3}\theta\right). \quad (26)$$

Finally, using the fact that f is also a function of ψ , we can write

$$\psi = g\left(r^{\frac{2}{3}} \sin\frac{3}{2}\theta\right), \quad (27)$$

where g is an unknown function. Rather than solving for g , though, we will apply matching between the inner solution and the boundary layer solution.

Before considering the flow in the boundary layer, we first analyze how the microstructure deforms with the fluid. Then as before, we can say that the fluid deforms like a line

element, but also in order to conserve mass, the fluid is squeezed in the direction perpendicular to the stretching,

$$\delta l \propto u \quad \delta l_{\perp} \propto \frac{1}{u}. \quad (28)$$

Following the work by Renardy (1994) we can then seek a solution of A in terms of the streamwise coordinates,

$$A = \lambda \mathbf{u}\mathbf{u} + \mu(\mathbf{u}\mathbf{v} + \mathbf{v}\mathbf{u}) + \nu \mathbf{v}\mathbf{v}, \quad (29)$$

where

$$\mathbf{u} = (u, v) \quad \mathbf{v} = \left(-\frac{v}{u^2 + v^2}, \frac{u}{u^2 + v^2} \right). \quad (30)$$

Note that $\mathbf{u} \cdot \mathbf{v} = 0$ and $|\mathbf{v}| = 1/|\mathbf{u}|$. We then substitute this construction into the upper convective derivative of A assuming that the flow is steady. We now include the effects of relaxation because they will be important in the boundary layer. After an excursion through the land of linear algebra, we find three equations for the unknowns λ, μ and ν ,

$$\mathbf{u} \cdot \nabla \lambda = 2 \frac{\dot{\gamma}}{u^2} \mu - \frac{1}{\tau} \left(\lambda - \frac{1}{u^2} \right), \quad (31)$$

$$\mathbf{u} \cdot \nabla \mu = \frac{\dot{\gamma}}{u^2} \nu - \frac{1}{\tau} \mu, \quad (32)$$

$$\mathbf{u} \cdot \nabla \nu = -\frac{1}{\tau} (\nu - u^2), \quad (33)$$

where the last equation is decoupled from the first two. It is helpful to note that

$$\dot{\gamma} = \mathbf{v} \cdot (\nabla \mathbf{u} + \nabla \mathbf{u}^T) \cdot \mathbf{u} = -u^2 \nabla \cdot \mathbf{v} \quad (34)$$

from which one can see that the terms that contain $\dot{\gamma}$ in (31) and (32) come from the $(A \cdot \nabla \mathbf{u} + (\nabla \mathbf{u})^T \cdot A)$ terms in the upper convective derivative. For slow flows, the inertia-like terms on the LHS are small, so the balance of the remaining terms gives,

$$\nu \sim u^2 \quad \mu \sim \gamma \tau \quad \lambda \sim \frac{1}{u^2} + \frac{2\gamma^2 \tau^2}{u^2}. \quad (35)$$

For fast flows, the RHS of (31–33) are approximately zero and therefore λ, μ and ν are constants.

In the boundary layer we can seek a similarity solution in streamline coordinates for the four unknown functions ψ, λ, μ and ν . Setting up this similarity solution is discussed in depth in Rallison and Hinch, 2004. At the conclusion of the analysis, the similarity function for ψ as we approach the outer limit of the boundary layer tends to $\xi^{7/3}$ where ξ is the non-dimensional parameter in the boundary layer. By matching the boundary layer solution to the inner elastic core, we find

$$\psi = Cr^{\frac{14}{9}} \sin^{\frac{7}{3}} \left(\frac{2}{3} \theta \right), \quad (36)$$

where C is an arbitrary constant. Finite element simulations [7] have shown excellent agreement with these results verifying that $u \sim r^{5/9}$ and $\sigma \sim r^{-2/3}$ as shown in figure 14.

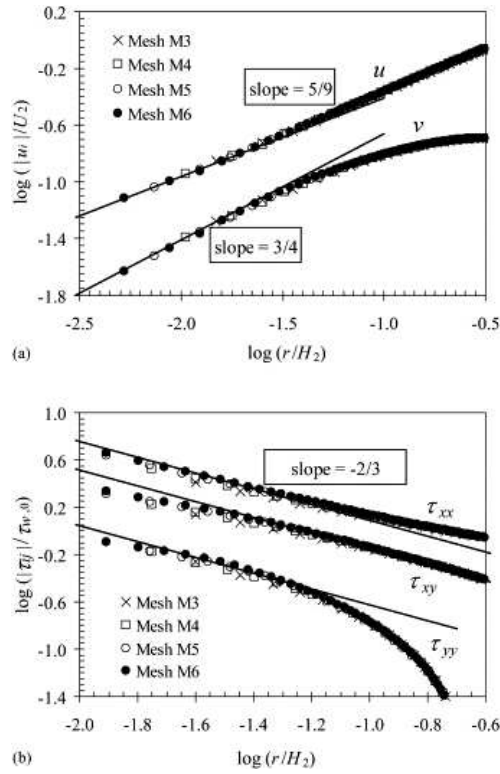


Figure 14: Finite element simulations of stress singularity at a sharp (270°) corner [7]. The upper plot shows velocity as a function of distance from the corner in the elastic core while the lower plot shows stress as a function of distance from the corner in the elastic core. The lines are drawn for reference to the power law relationships.



Figure 15: A filament being stretched.

4 Elastic stress saturation in a stretching filament

We will now look at the problem of rapid stretching of a filament of an elastic liquid, with a large surface tension. The problem is motivated from the fiber spinning process, in which fibers are drawn rapidly from droplets of viscoelastic liquids.

Let $a(t)$ be the radius of the filament at time t (see figure 15). Also, let the strain rate applied to the filament be $E(t)$. Conservation of mass gives us

$$\dot{a} = -\frac{1}{2} E a \quad (37)$$

Hoop stress due to surface tension (χ) has the effect of squeezing the filament. Thus, with neglect of the viscous stresses and the elastic stress component, σ_{rr} , conservation of momentum leads to

$$\frac{\chi}{a} = G A_{zz} \quad (38)$$

where A is the tensor describing the configuration of the microstructure and G is the elastic modulus.

Due to the straining of the filament, the microstructure will get deformed with time. Here we model the microstructure with an Oldroyd-B model, assuming large deformations of the microstructure, and get

$$\begin{aligned} \dot{A}_{zz} &= 2EA_{zz} - \frac{1}{\tau} A_{zz} \\ &= (2E - \frac{1}{\tau}) A_{zz}, \end{aligned} \quad (39)$$

where τ is the relaxation time of the microstructure. Since the surface tension is resisting the stretching of the filament, we need to find out the strain E required to stretch the filament. The strain rate cannot be very large because that would break the filament. Equation of momentum, Eq. 38, gives $A_{zz} \propto \frac{1}{a}$. Using this and Eq. 37, we have $\frac{\dot{A}_{zz}}{A_{zz}} = -\frac{\dot{a}}{a} = \frac{1}{2} E$. We then look at Eq. 39 and solve to get $E = \frac{2}{3} \frac{1}{\tau}$. Conservation of mass (Eq. 37) then gives the variation of filament radius with time as:

$$a(t) = a(0) e^{-\frac{t}{3\tau}}. \quad (40)$$

The result we have obtained does not compare well with experiments, in the as is shown in figure 16. The experiments were done using S1 fluid by Liang and Mackley [8] and the solid theoretical curves are from the analysis carried out by Entov and Hinch [9] in which they used a spectrum of relaxation times instead of the single relaxation time that we used in our earlier derivation. When a spectrum of relaxation times is used for the microstructure, the solution for the stretching and relaxation of stress is:

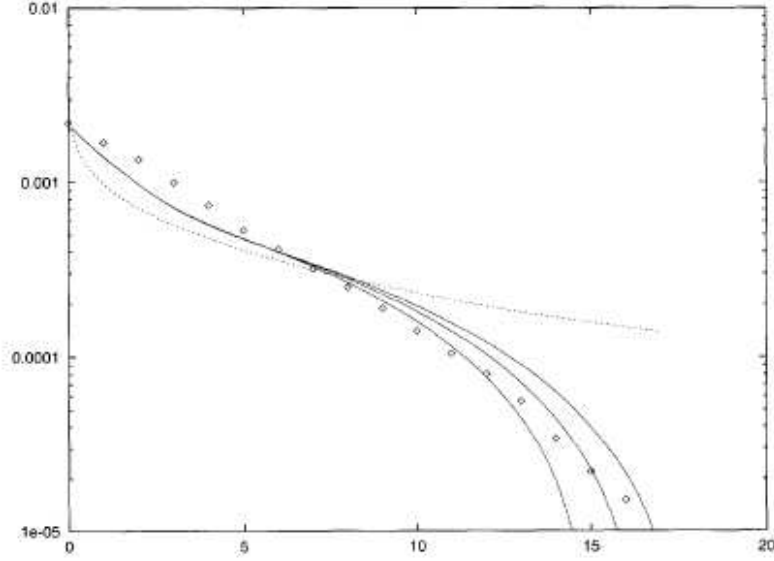


Figure 16: Variation of the diameter of an S1 liquid filament (on y-axis) being stretched with time (on x-axis). The dotted line is the theoretical result derived in Eq. 40.

$$A_{zz}^i = \frac{1}{a^4(t)} e^{-t/\tau_i}, \quad (41)$$

where the subscript i represents the relaxation mode.

Hence, the momentum equation becomes

$$\frac{\chi}{a} = \frac{1}{a^4} \sum_i g_i e^{-t/\tau_i}. \quad (42)$$

Then, the radius of the filament as a function of time is

$$a(t) = \left(\frac{G(t)}{\chi} \right)^{1/3} \quad (43)$$

where $G(t) = \sum g_i e^{-t/\tau_i}$ is the material stress-relaxation function.

5 Oldroyd-B: Successes and Failures

The Oldroyd-B is one of the simplest and the most frequently used models for the microstructure. Its simplicity lies in the fact that it adds an elasticity G to the fluid and a single relaxation time τ , over and above the Newtonian fluid viscosity, μ_0 . Although this model has been successful in explaining some of the viscoelastic phenomena, it has been found to perform poorly when the rate of deformation of the fluid is much larger than the relaxation time of the microstructure.

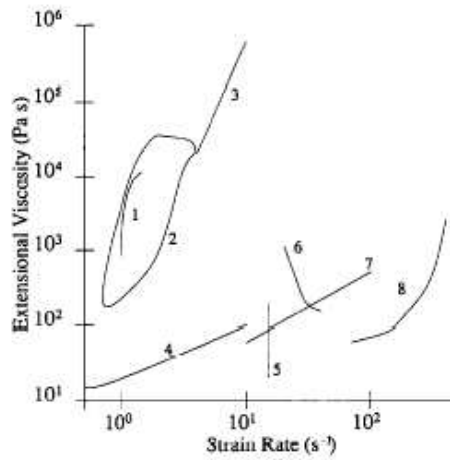


Figure 17: Extensional viscosity of an M-1 fluid depends on what device you use to measure it.

Figure 17 demonstrates this problem quite vividly. This is a plot of measurements of extensional viscosity of the same fluid (M1) but in different devices which are represented by different curves labeled 1 through 8. Curve 1 is from an open siphon device, 2 is from a spinline, 3, 7 & 8 are from a contraction flow device, 4 is from an opposing jet, 5 is from a falling drop and 6 is from a falling blob. The other plots in figure 17 are details of some of the measurements made. Notice the large scatter and disagreement in the curves. This raises two questions. First, is extensional viscosity an appropriate quantity to be measured for non-Newtonian fluids or should we be using some other measure for the influence of a largely deformed microstructure on the flow, e.g. elastic constant? Second, will Oldroyd-B be able to capture the effect of largely extended microstructures on the flow?

The answer to the first question is not clear at this time. Using the strain on the microstructure to define the stress with the help of an elastic constant could be one way of going about it. The answer to the second question is that Oldroyd-B fails to describe these effects. For a contraction flow, while Oldroyd-B does predict a small initial decrease in pressure drop, it fails to predict the large increase in pressure drop or the size of upstream vortices seen at higher flow rates. In the case of a fluid flowing past sphere, it rightly predicts the initial decrease in drag but again fails to predict the increase in force and large wake lengths observed at higher flow rates. As a final example, Oldroyd-B gives us the correct time scale for the deformation of capillary filament being stretched, but does not predict any breakage of the filament at very high applied strain rates. From a numerical perspective, the Oldroyd-B model runs into problems for high De , because it suggests that the microstructure can keep stretching to infinite lengths as long as there exists a force to deform it. Consequently, the extensional stresses become negative beyond a critical De . This is obviously unrealistic and we are forced to conclude that more physics is required in the constitutive equation than contained in Oldroyd-B.

The modification to the constitutive equation that has been successfully used and rather swiftly accepted is FENE — Finitely Extensible Non-Linear Elastic microstructure. This

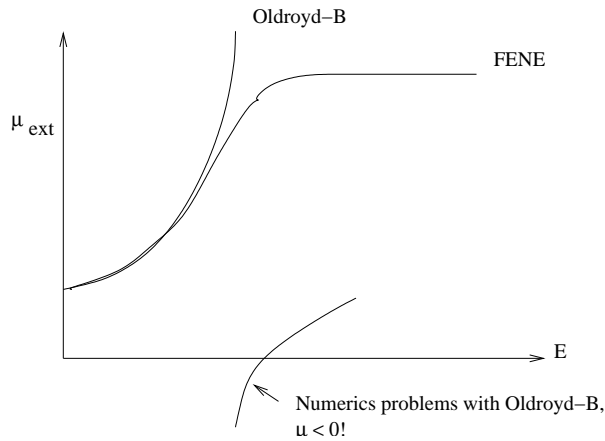


Figure 18: The negative viscosity as predicted by Oldroyd-B and the FENE cure to that.

model limits the deformation to a certain length L and retains a large positive value for extensional stresses at high De . It predicts a large pressure drop for strong contraction flows, a large increase in drag for strong flows past a sphere and finally, breakage of the capillary filament when drawn at a large strain rate. Also, for strongly extensional flows in general, the FENE modification predicts $\mu_{ext} \gg \mu_{shear}$. This dramatic anisotropy in viscosity can be of direct consequence to polymer turbulent drag reduction.

In conclusion, we can say that we have begun to get some understanding of both the strong and weak flows of elastic liquids. While the Oldroyd-B model is a good choice for small $De \ll 1$ flows, the FENE model is a clear winner for high $De \gg 1$ flows. Thus Non-Newtonian fluids have unique dynamical signatures that cannot be explained by the superposition of viscous and elastic effects. A general theory for such fluids is still lacking due to the diversity of materials and their characteristic flow behaviors.

Notes by Anshuman Roy and Andrew Thompson

References

- [1] M. D. Chilcott and J. M. Rallison, “Creeping flows of dilute polymer solutions past cylinders and spheres,” *Journal of Non-Newtonian Fluid Mechanics* **29(1-3)**, 381 (1988).
- [2] V. Tirtaatmadja, P. H. T. Uhlherr, and T. Sridhar, “Creeping motion of spheres in fluid m1,” *Journal of Non-Newtonian Fluid Mechanics* **35(2-3)**, 327 (1990).
- [3] O. G. Harlen, E. J. Hinch, and J. M. Rallison, “Birefringent pipes - the steady flow of a dilute polymer solution near a stagnation point,” *Journal of Non-Newtonian Fluid Mechanics* **44**, 229 (1992).
- [4] P. Szabo, J. M. Rallison, and E. J. Hinch, “Start-up of flow of a fene-fluid through a 4:1:4 constriction in a tube,” *Journal of Non-Newtonian Fluid Mechanics* **72**, 73 (1997).

- [5] U. Cartalos and J. M. Piau, “Creeping flow regimes of low concentration polymer solutions in thick solvents through an orifice die,” *Journal of Non-Newtonian Fluid Mechanics* **45**, 231 (1992).
- [6] H. Lamb, *Hydrodynamics* (Cambridge University Press, Cambridge, UK, 1932).
- [7] M. A. Alves, P. J. Oliveira, and F. T. Pinho, “Benchmark solution for the flow of oldroyd-b and ptt fluids in planar contractions,” *Journal of Non-Newtonian Fluid Mechanics* **110**, 45 (2003).
- [8] R. F. Liang and M. R. Mackley, “Rheological characterization of the time and strain dependence for polyisobutylene solutions,” *Journal of Non-Newtonian Fluid Mechanics* **52(3)**, 387 (1994).
- [9] V. M. Entov and E. J. Hinch, “Effect of a spectrum of relaxation times on the capillary thinning of a filament of elastic liquid,” *Journal of Non-Newtonian Fluid Mechanics* **72(1)**, 31 (1997).